Graphene Oxide—Periodic Mesoporous Silica Sandwich Nanocomposites with Vertically Oriented Channels

Zheng-Ming Wang,[†,§] Wendong Wang,[†] Neil Coombs,[‡] Navid Soheilnia,[†] and Geoffrey A Ozin[†,*]

[†]Materials Chemistry Research Group and [‡]Center for Inorganic and Polymeric Nanomaterials, Chemistry Department, 80 St. George Street, University of Toronto, Toronto, Ontario, Canada M5S 3H6 and [§]Energy Technology Research Institute, National Institute of Advanced Industrial Science and Technology, 16-1 Onogawa, Tsukuba, Ibaraki 305-5869, Japan

ABSTRACT This paper describes the synthesis and characterization of single-layer graphene oxide—periodic mesoporous silica sandwich nanocomposites. Through a comprehensive exploration of the synthesis conditions, it has proven possible to create the first example of a graphene oxide—periodic mesoporous silica nanocomposite in which hexagonal symmetry PMS film grows on both sides of the graphene oxide sheets with the mesoporous channels vertically aligned with respect to the graphene oxide surface. The formation of this novel architecture is found to be very sensitive to pH, the ratio of surfactant template to graphene oxide, the amount of silica precursor, and the temperature of the synthesis. On the basis of the collected data of a multi-technique analysis, it is proposed that the mode of formation of the nanocomposite involves the co-assembly of silicate—surfactant admicelles on opposite sides of graphene oxide platelets acting thereby as a template for growth of vertical mesopores off the platelet surface. These composites showed semiconductive behavior with electrical conductivity sensitively responding to analyte vapor exposure. The discovery of graphene oxide—periodic mesoporous silica sandwich nanocomposites will provide new opportunities for research that exploits the synergism of the graphene oxide and periodic mesoporous silica parts.

KEYWORDS: graphene oxide · periodic mesoporous silica · nanocomposite · vertically aligned pore

Since the discovery in 1996 that films of surfactant-templated hexagonal symmetry periodic mesoporous silica (PMS) could be grown on substrates like mica[1] and graphite[2,3] with their channels oriented parallel to the substrate surface, there has been intense global research activity on these films along a number of directions in chemistry and physics, materials science, and engineering. These include efforts to extend the scope of the synthesis to other templates, substrates, pore morphologies, and compositions,[4] to understand the mode of formation,[5] to determine what synthesis and substrate parameters control the alignment of channels either parallel or perpendicular to the surface of the substrate,[6−9] to define and control the type and population of defects,[10] and to explore the utility of these films in a number of application areas that include low refractive index optical waveguides,[11] anti-reflection coatings,[12] low-*k* microelectronic packaging,[13−15] photonic crystal chemical sensing,[16] and nanofluidics.[17]

In the context of the synthesis of PMS on graphite and mica, the original proposal for the mode of film formation at the solution−substrate interface has not changed. In brief, pristine graphite and mica, respectively, present hydrophobic and hydrophilic surfaces to the synthesis solutions which often comprise a cationic surfactant template, silicate precursor, acid or base silicate condensation−polymerization catalyst, water, and ethanol. Under these conditions, the hydrophobicity of the graphite surface drives the surfactant template to form regular arrays of parallel aligned hemimicelle cylinders registered with the primary three-fold axes of the hexagonal symmetry lattice of graphite, a process dubbed meso-epitaxy. These hemimicelle cylinders serve as a template to direct the formation of silicate−surfactant micelle cylinders thereupon (*i.e.*, the silicatropic mesophase), which undergo hydrolytic polycondensation to form a PMS film with channels oriented parallel to the graphite substrate. By contrast, the hydrophilicity of the mica surface coerces the surfactant template to form regular arrays of parallel aligned micelle cylinders registered with the primary three-fold axes of hexagonal symmetry lattice of mica, which direct the formation of silicate surfactant micelle cylinders thereupon and undergo hydrolytic polycondensation to form a PMS film with channels oriented parallel to the mica substrate.

The only distinguishing feature between the PMS film that forms on graphite and mica is the monolayer surfactant template that self-assembles at the substrate−solution

*Address correspondence to gozin@chem.utoronto.ca.

Received for review October 2, 2010 and accepted November 16, 2010.

Published online November 23, 2010. 10.1021/nn102618n

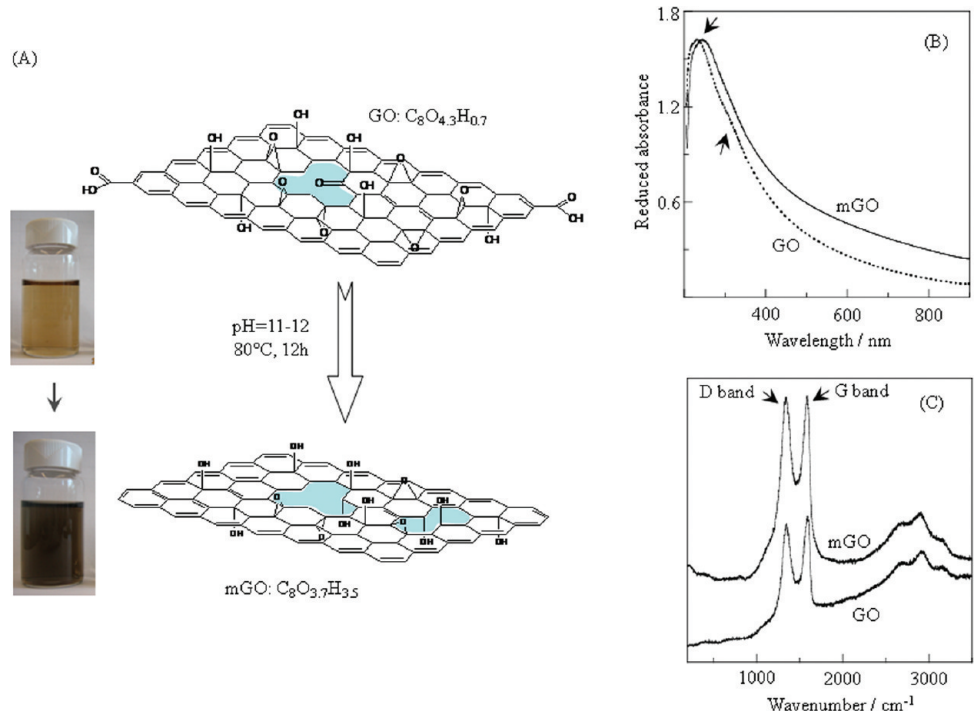

Figure 1. (A) Schematic diagram of GO modification, (B) UV−vis, and (C) Raman spectra before and after GO modification.

interface, namely, a hemimicelle cylinder on graphite compared to a micelle cylinder on mica. The difference arises from the energetic advantage of the surfactant (*e.g.*, cetyltrimethylammonium chloride, CTACl) to bind to graphite with its alkane tail parallel to the surface encouraged by the stabilizing surface hydrophobic effect in conjunction with cationic surfactant headgroup image charge and ion-pair effects, thereby favoring the formation of parallel aligned surfactant hemimicelle cylinders. On mica, the surfactant cationic headgroup prefers to bind to anionic surface sites with the surfactant alkane tail perpendicular to the surface, thereby favoring the formation of parallel aligned surfactant micelle cylinders.

These models for the formation of oriented and registered PMS film on structurally well-defined hydrophobic and hydrophilic surfaces raise the very interesting question, what happens to PMS grown on graphene and graphene oxide (GO) surfaces? These substrates are especially fascinating as their surface polarity can be tuned by the extent of chemical oxidation and reduction, respectively;[18−21] they can be made colloidally stable with a thickness of nanometers, and both sides are accessible for PMS film growth.

In the research described herein, we present a detailed study of the growth of PMS film on controlled polarity GO platelets comprising just a single layer. Synthesis conditions have been established that favor the formation of reduced graphene oxide (rGO)−PMS sandwich nanocomposites having the distinctive structural feature that the channels are found to grow perpendicularly off both surfaces of the GO platelets. These composites show an interesting semiconductive behavior and sensing property toward analyte vapor due to the unique structure. On the basis of the collected results of a multi-technique analysis, a possible model is proposed that can rationalize this interesting and surprising observation.

RESULTS AND DISCUSSION

GO Modification. Although treatment in basic conditions is usually employed to modify the surface chemistry of carbon and to increase the population of functional groups on carbon materials,[22] recent reports on the mild treatment of GO under basic conditions demonstrate the reduction of GO with a loss of certain functional groups and concomitant partial restoration of the graphene hexagonal structure.[23,24] Color changes of GO dispersions from clear brown to dark gray after our chosen treatment (Figure 1A) suggest a change of carbon structure in the colloidal solution, which can be probed by UV−vis and Raman spectroscopy. As shown in Figure 1B, the UV−vis spectrum of GO dispersion before treatment shows a main absorption peak centered at 226 nm and a weak shoulder around 300 nm, which are assigned to the $\pi\rightarrow\pi^*$ transition of aromatic −C═C− and the $n\rightarrow\pi$ transition of carbonyl or carboxyl −C═O groups, respectively. The wavelength of the $\pi\rightarrow\pi^*$ absorption is smaller, and the intensity of $n\rightarrow\pi$ absorption seen as a shoulder is much weaker as compared to those GO from a modified Hummer's method (which is usually around 231 nm for $\pi\rightarrow\pi^*$ absorption),[24−26] indicating that the GO obtained contains a lower population of conjugated C═C bonds and a smaller amount of carbonyl or carboxyl groups. After treatment, the peak of the $\pi\rightarrow\pi^*$ absorption batho-

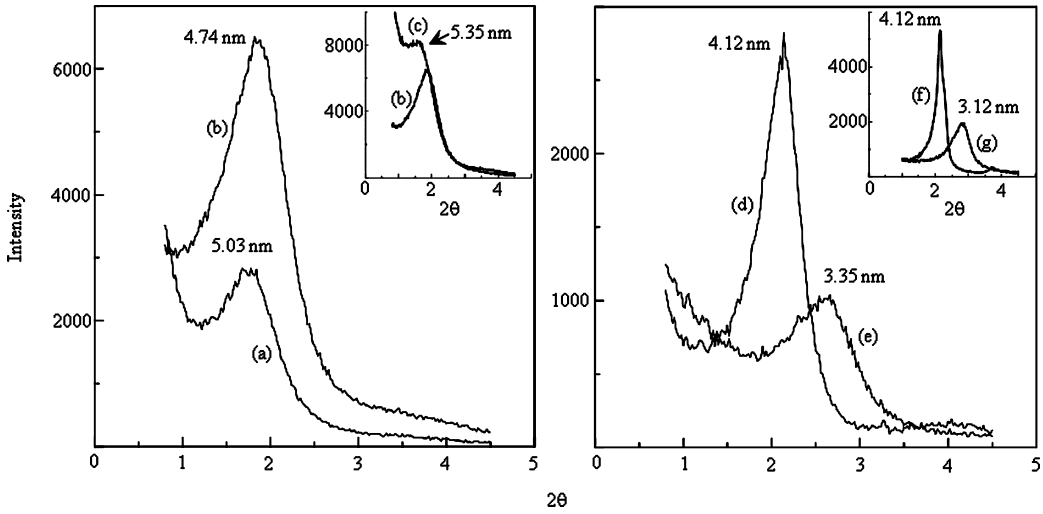

Figure 2. PXRD patterns of (a) mGO−PMS(0.27), (b) rGO−PMS(0.27), and (c) CMS (after pyrolysis) prepared at pH 11.7, and (d) mGO−PMS(0.27), (e) rGO−PMS(0.27), and CMS (before (f) and after (g) pyrolysis) prepared at pH 12.7.

chromically shifted to 245 nm accompanied by an overall increase of the background absorption at wavelengths above 240 nm, indicative of carbonization or partial restoration of the conjugated π structure in modified GO (what we denote mGO). This behavior agrees with the reported results with the slight difference that the π→π* transition occurs at a lower wavenumber, which can be attributed to the milder modifying conditions used as compared to the more severe ones in the literature using strong reductants.[25] The shoulder around 300 nm becomes less apparent after treatment, implying significant reduction in the amount of carbonyl or carboxyl −C═O groups by the treatment, in good agreement with the FT-IR result (Supporting Information Figure S1). The restoration of conjugated aromatic −C═C− bonds by the treatment is also supported by Raman spectra. As shown in Figure 1C, the G-band position of GO around 1602 cm^{-1} is slightly red-shifted to 1595 cm^{-1} in mGO, which is in the direction toward a more perfect graphene structure.[27,28] However, a small increase in the intensity of the D-band around 1346 cm^{-1} was observed after the treatment, which was also reported in the literature for other reduced GO.[29,30] Since the D-band is diagnostic of a breathing mode of aromatic rings and needs defects for activation,[31] this increase in the D-band intensity suggests a slight increase of defect holes or cracking of larger layers to smaller ones due to the treatment.

The above results suggest that the GO modification process involves reaction/reduction of surface oxygen-containing groups (carboxyl, alcohol, and epoxy groups in the Lerf−Klinowski model[32] or quinone phenol groups in the Scholz−Boehm[33] and Dekany's models[34]). The following information further helps to understand the observed behavior. First, as shown in Figure 1A, the oxygen content of mGO is not markedly decreased as expected, whereas the mGO concentration after reduction is decreased by ~32% as compared to the parent GO dispersion. This decrease in weight is independent of the original GO concentration and cannot be explained simply by the decrease in the amount of oxygen. Second, TGA measurements (Supporting Information Figure S2) clearly show that thermal decomposition of surface functional groups on GO usually occurs around 453 K in agreement with previous reports.[35] However, this decomposition step is insignificant for mGO. Third, the pH value slightly decreases after reduction particularly for higher GO concentrations, indicative of the consumption of hydroxide ions OH^- in solution during the reaction. Therefore, the treatment of the GO experienced a complicated surface chemical process which involves a loss of carbon and a possible redistribution of oxygen-containing groups on GO. FT-IR results (Supporting Information Figure S1) show that plenty of C−OH groups still remain after the treatment, which are likely responsible for the colloidal stability of dispersions of mGO in water.[36] Figure 1A outlines the solution phase process of chemical modification of GO and illustrates the possible formation of defect holes and rearrangement of the surface group on mGO platelets.

Nanocomposites. It has been reported that a single-layer GO dispersion can be realized in the concentration range below 4 mg/mL.[18] We have applied atomic force microscopy (AFM) to examine the mGO platelets spin-coated on a silicon wafer by using the colloidally stable mGO dispersion prepared from 1 mg/mL GO solution. The result showed mGO platelets with thickness of 0.8 to 1.2 nm, which ascertains the single-layer dispersion properties of these mGO solutions. While adding CTACl into the mGO dispersion maintains good colloidal stability, the addition of TEOS and subsequent reaction leads to formation of a new product phase. The denser, darkly colored phase was readily collected by centrifugation and is representative of our designated

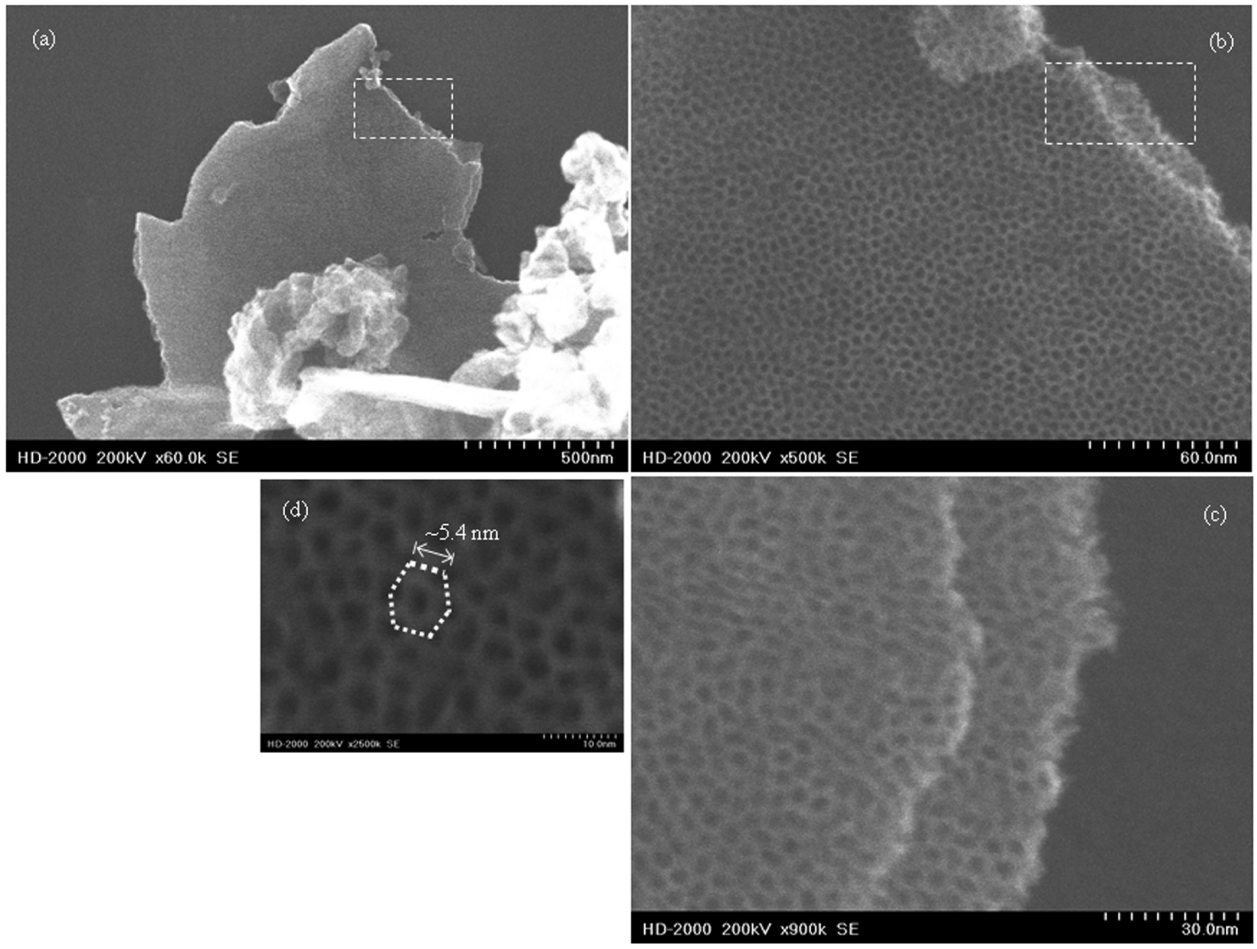

Figure 3. SEM images of rGO−PMS(0.27) prepared at pH 11.7 recorded in SE mode using the Hitachi HD-2000 STEM operating at 200 kV. (b,c) Expansions of the frame areas in (a) and (b), respectively, and (d) hexagonal array with interpore distance (~5.4 nm) very close to that from PXRD ($2d_{100}/\sqrt{3}$).

mGO−PMS(*x*) nanocomposite product. Figure 2 shows the PXRD patterns of mGO−PMS(0.27) and the derived rGO−PMS(0.27) for comparison with the control mesoporous silica (CMS) samples, the latter of which were synthesized under the same conditions but without mGO. The nanocomposites showed diagnostic diffraction peaks with *d* spacing around 3.35−5.03 nm. They are assigned to d_{100} PXRD reflections from hexagonally ordered PMS. The degree of order of the PMS structure of these nanocomposites is very sensitive to the chosen pH value, as evidenced by differences in their PXRD patterns. On the one hand, the nanocomposite prepared at pH 11.7 (Figure 2a,b) showed a greater d_{100} spacing (5.03 and 4.73 nm), and the intensity of the 100 peak was greater after thermal treatment. The contraction of the d_{100} spacing caused by thermal treatment is however very small (0−0.3 nm), indicative of formation of a rigid mesopore structure. The weak diffraction peak of the CMS control sample synthesized without mGO (Figure 2c) demonstrated that the synthesis conditions chosen were not favorable for the growth of a well-formed PMS structure. The result of the control synthesis indicates that mGO has a distinctive structure-directing impact on the formation of the PMS. On the other hand, pH 12.7 is a suitable condition for obtaining a well-formed PMS in solution (Figure 2f,g). The nanocomposite prepared at pH 12.7 (Figure 2d,e) showed a similar pattern to the CMS control sample (Figure 2f,g). After thermal treatment, the intensity of the diffraction peak was greatly reduced and a dramatic contraction in d_{100} spacing (0.8−1.1 nm, 1 nm for CMS) was observed, indicative of an unstable PMS structure.

It is noteworthy that no second-order diffraction peak was observed in the PXRD patterns of the nanocomposites, suggesting that the PMS does not exhibit long-range order. While a perfect PMS structure usually shows a smaller d_{100} spacing (~4.1 nm), d_{100} spacing (5.03 nm) of mGO−PMS(0.27) (pH 11.7) is greater even than that of the reported pristine PMS with poorly ordered hexagonal channels (for example, 4.5 nm for the as-synthesized spherical PMS[37]). However, the striking characteristic of this material is that the contraction of its d_{100} spacing upon pyrolysis is among the smallest so far reported (0.3 nm for MCM41,[38,39] 0.1−0.3 nm for PMS on graphite,[2] 0.3−0.6 nm PMS on mica,[1] 0.2−0.5 nm for PMS on air−liquid interface,[40] 0.4−0.5 nm for

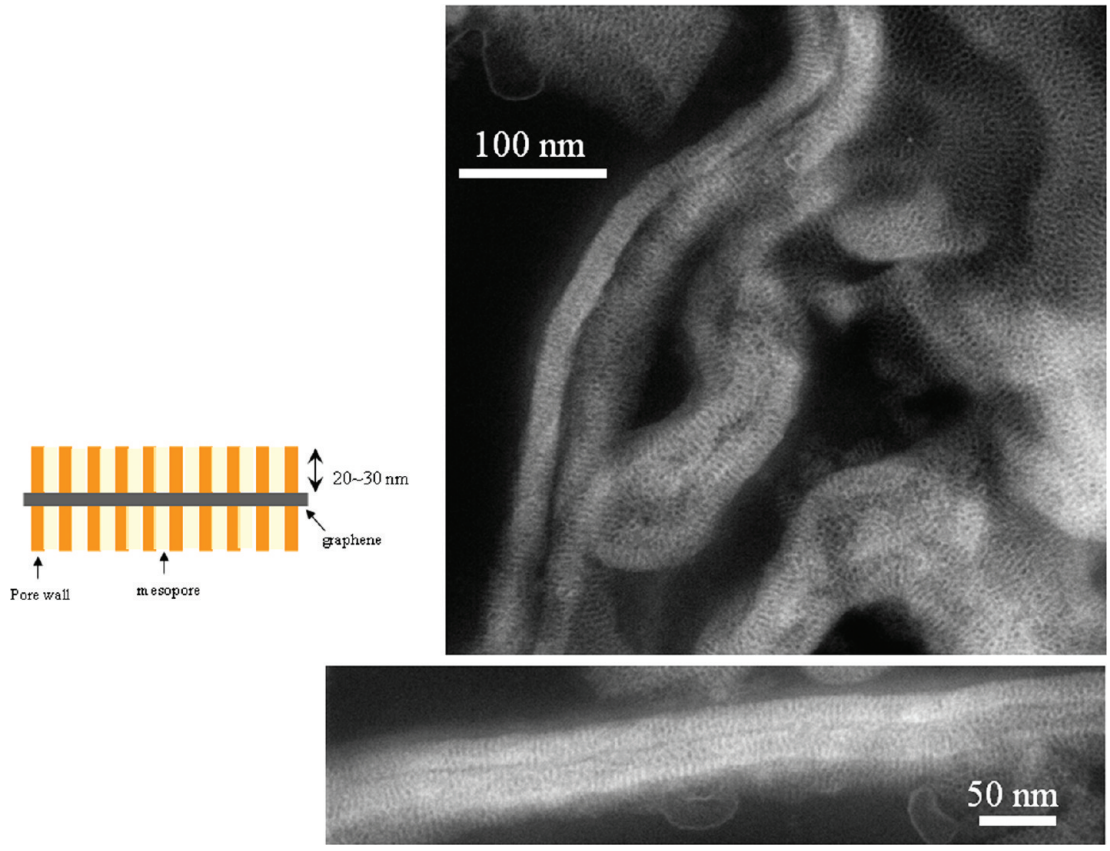

Figure 4. Microtome STEM pictures of rGO−PMS(0.27) prepared at pH 11.7, which clearly shows rGO sheets sandwiched by arrays of vertically aligned mesopores having heights of 20−30 nm.

silicate−surfactant lyotropic crystal[41]), indicating that a well-polymerized rigid PMS structure has been formed before the removal of the surfactant template.

In the TEM and SEM pictures of rGO−PMS(0.27) (pH 11.7), only platelet morphology was observed and almost all of the platelets are covered by a mesopore structure. As an example, Figure 3a shows an image of an aggregate of flat platelets with an irregular shape (maximum width × length: 1.2 μm × 1.2 μm), the expansion of which clearly displayed that the whole surface of the top platelet was covered in mesopores. The expanded images on the edge (Figure 3b,c) evidence the stacking of layers with the surface of the second (back) layer still covered by mesopores. A high-resolution image (Figure 3d) confirmed that the mesopore structure is an imperfect hexagonal array with an interpore distance around 5.4 nm, a value very close to that calculated from the d_{100} spacing obtained by PXRD ($2d_{100}/\sqrt{3}$), with pore size around 3−4 nm. As the platelet mesoporous structure/morphology unveiled by these images is quite different from the usual pure PMS, it is likely that the channels of these mesostructures are vertically grown off an underlying mGO/rGO layer. In order to investigate this further, a high-resolution TEM image was recorded using 20−100 nm thickness ultramicrotomed samples. As shown in Figure 4, these images strongly suggest the presence of rGO sheets sandwiched by arrays of vertically aligned mesopores. The presence of a rGO sheet was further confirmed by cross-sectional elemental mapping, although it proved challenging to accurately determine the carbon layer thickness in this way (Supporting Information Figure S3). The height of the mesoporous channels in the so-formed rGO−PMS(0.27) sandwich can be estimated to be 20−30 nm despite that the cross-sectional image in the TEM micrographs is unlikely to be exactly perpendicular to the sheet direction. In sharp contradistinction, Figure 5 depicts TEM images of rGO−PMS(0.27) (pH 12.7) from which it is not possible to detect the same vertically aligned mesopore structure observed in rGO−PMS(0.27) (pH 11.7). What was observed instead is worm-like mesopore morphology of the kind usually ascribed to poorly ordered, pristine mesoporous silica formed either in separate domains or in association with plate-like aggregates with the mesoporous structure hardly differentiated. A comparison of TEM images indicates that the PMS structure in rGO−PMS(0.27) (pH 12.7) was less influenced by the carbon surface, but the structure in rGO−PMS(0.27) (pH 11.7) was formed with the mGO platelet as the template.[42] In addition, the distinct mesopores and channel walls observed in the TEM images of rGO−PMS(0.27) suggest that the top and bottom PMS films on opposite sides of the platelet were in registry (Supporting Information Figure S4). In other words, there seems to be little or no offset between the meso-

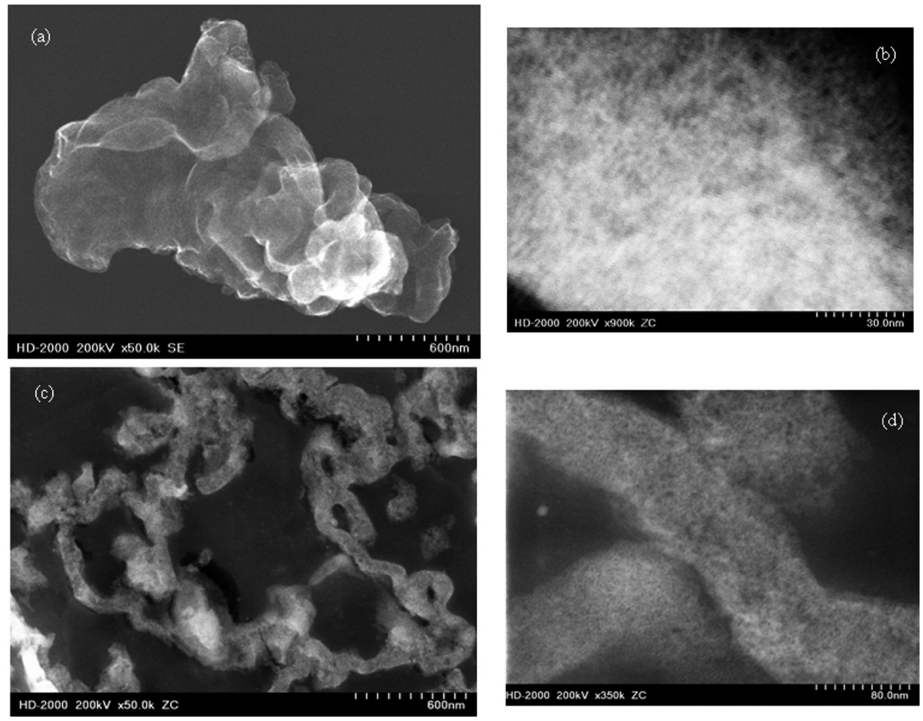

Figure 5. STEM pictures of rGO−PMS(0.27) prepared at pH 12.7, which shows lots of worm-like morphology usually known for less ordered pure PMS materials, either separated from or loaded on carbon platelets. No clear vertically aligned mesopores were observed as in samples prepared at pH 11.7: (a) platelet aggregates, (b) expansion of one portion of the surface in (a) showing ill-defined parallel channels, (c,d) separated particles and its expansion.

structures above and below the rGO sheet. FFT analysis of TEM images supports this observation with an interpore distance of approximately 5 nm.

The mesoporosity of the nanocomposites was characterized further by N_2 adsorption. Figure 6a shows the N_2 adsorption isotherms at 77 K on rGO−PMS(0.27) and the corresponding CMS materials. In comparison with CMS (pH 11.6), where an ordered mesoporous structure was not well-evolved, rGO−PMS(0.27) (pH 11.7) with its remarkable PMS structure exhibits an enhanced adsorption. Its adsorption isotherm is typical of type IV,[43,44] showing an inflection in adsorption around $P/P_0 = 0.3-0.4$. A less abrupt inflection means a wider pore size distribution as compared to perfect PMS materials.[38,45] Although no hysteresis was observed in the inflection range of sorption, similar to that found with the pristine PMS materials, the adsorption isotherm does show a small hysteresis typical of type H3

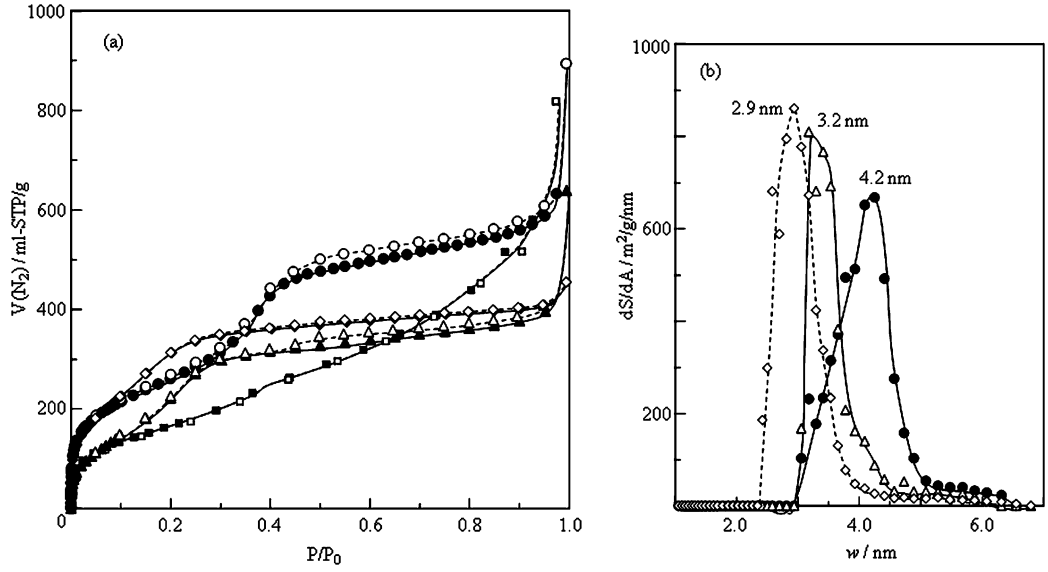

Figure 6. (a) Adsorption isotherms at 77 K on rGO−PMS(0.27) prepared at pH 11.7 (●, ○) and 12.7 (▲, Δ) and CMS prepared at pH 11.7 (■, □) and 12.7 (◆, ◇). Filled and unfilled marks are the adsorption and desorption branches, respectively; (b) pore size distribution from DFT method.

TABLE 1. Mesopore Parameters

sample	S_{BET} [a] (m^2/g)	S_{BET}*[b] (m^2/g)	S_{DFT} (m^2/g)	$V_{0,DFT}$ (mL/g)	D_{DFT} (nm)
rGO−PMS(0.27) (pH 11.7)	925	770	740	0.762	4.2
rGO−PMS(0.27) (pH 12.7)	760	630	560	0.509	3.2
CMS (pH 12.5)	1035	860	725	0.566	2.9

[a]From $\sigma_{N2} = 0.162$ nm^2, P/P_0 range = 0.05−0.1.[49] [b]From $\sigma_{N2} = 0.135$ nm^2, P/P_0 range = 0.05−0.1.[49]

or H4 at $P/P_0 > 0.45$, characteristic of an assembly of plate-like particles.[46] In conjunction with the increased adsorption around $P/P_0 = 1$, these phenomena indicate a porous architecture in which rGO−PMS sandwiched platelets aggregate together to form secondary mesopores and/or macropores and thereby increase the external surface area. On the other hand, the isotherm of rGO−PMS(0.27) (pH 12.7) showed the mesopore inflection at a lower P/P_0 range than that of rGO−PMS(0.27) (pH 11.7), indicative of a different pore system. The shape of its adsorption isotherm is similar to that of CMS (pH 12.5), but with a reduced amount of adsorption. The pore size distributions (PSDs) of the samples were analyzed using the nonlocalized density functional theory (NLDFT) method based on a metastable spinodal pore condensation model from adsorption branches.[47,48] As expected from the shape of its isotherm, rGO−PMS(0.27) (pH 11.7) exhibits a comparatively wide PSD (3−5 nm in Figure 6b) with an average pore width of 4.2 nm. By contrast, rGO−PMS(0.27) (pH 12.7) shows a narrower PSD and a smaller pore width. The existence of carbon platelets in this sample causes a slight increase in the mesopore size compared to the pure CMS (pH 12.5). Table 1 summarizes for all samples the values of specific surface area, S_{BET} and S_{BET}*, from the Brunauer−Emmett−Teller (BET) method and specific surface area, S_{DFT}, pore volume, $V_{0,DFT}$, and average pore width, D_{DFT}, from the NLDFT method.[49]

Synthesis Conditions and Zeta Potential. In order to explore the mode of formation of these novel rGO−PMS sandwich nanocomposites, synthesis conditions were varied and optimized. An investigation of the effect of a wider range of pH (2−11.7) showed that it is possible to obtain the PMS structure from pH 7 to 11.7, whereas the optimum pH range is around 11−12 (Supporting Information Figure S5a). The PMS structure disappeared in the range of pH <6 but appeared again at pH 2.0 (the isoelectric point of silica). Control syntheses (using the same procedures, conditions, and reagent amounts but without mGO) produced only a clear solution in the range of pH <10 or pH >13, amorphous powder precipitated from pH 11, and the PMS structure was formed around pH 12.5. These results are consistent with a literature report.[50] Thus, mGO sheets play a crucial role in forming the PMS structure in rGO−PMS nanocomposites at pH <12, in particular, at pH <11. The poorer PMS structure at pH <11 is caused by the insufficient condensation polymerization of silicate oligomers under less basic conditions unfavorable for the deprotonation of surface silanol groups. Examination of the effect of CTACl and GO content on the synthesis revealed the existence of optimum values, ranging around 29−80 mM for CTACl (Supporting Information Figure S5b) and around 0.27−0.54 mg/mL for GO (Supporting Information Figure S5c), which indirectly shows the importance of the interaction between CTACl molecules and mGO layers on the formation of the PMS structure. Higher amount of TEOS tends to form a poorer quality PMS structure as these conditions favor the formation of amorphous silica phase at pH ≤11.7 (Supporting Information Figure S5d). A lower reaction temperature proves to be unfavorable for the formation of a better PMS structure because of a low polymerization reaction rate of silicate oligomers (Supporting Information Figure S5e).

Zeta potential measurements were carried out in order to investigate the interaction between CTACl molecules and mGO layers. As shown in Figure 7A, single layers of mGO showed a negative zeta potential (−37 to −40 mV) in the range of pH 5−12, consistent with the formation of a stable negatively charged colloidal dispersion. The colloidally stable range of mGO is slightly wider than that of the parent GO. Increasing pH >10 slightly increased the zeta potential, indicating that there exists some surface groups which possess a high pK_b value and that can dissociate at higher pH. A further increase in pH >12 destabilized the mGO dispersion, and a sudden decrease in zeta potential at pH >13 was accompanied by the formation of precipitates in the solution. When CTACl is added into the mGO dispersion, a stable colloidal dispersion is still formed but surprisingly now exhibits a large positive zeta potential (Figure 7B, shown in the range of pH 9−13). Since the zeta potential of pure CTACl solution is negligible in the same range (Figure 7A), the negative to positive charge inversion of the zeta potential is clear evidence of the adsorption of CTACl aggregates on the surface of mGO, and which are responsible for the colloidal stability of the single layers of mGO in solution. The notable increase in zeta potential at higher temperature is attributable to the increase in the adsorption of CTACl *via* a chemical process such as ion exchange. As shown in Figure 7C, an increase in CTACl concentration leads to an increase in zeta potential by increasing CTA^+ adsorption, reaching saturation around 20−100 mM. The decrease in zeta potential beyond 100 mM and at pH >12 (at 348 K) can be attributed to the decrease in CTACl adsorption on mGO layers due to

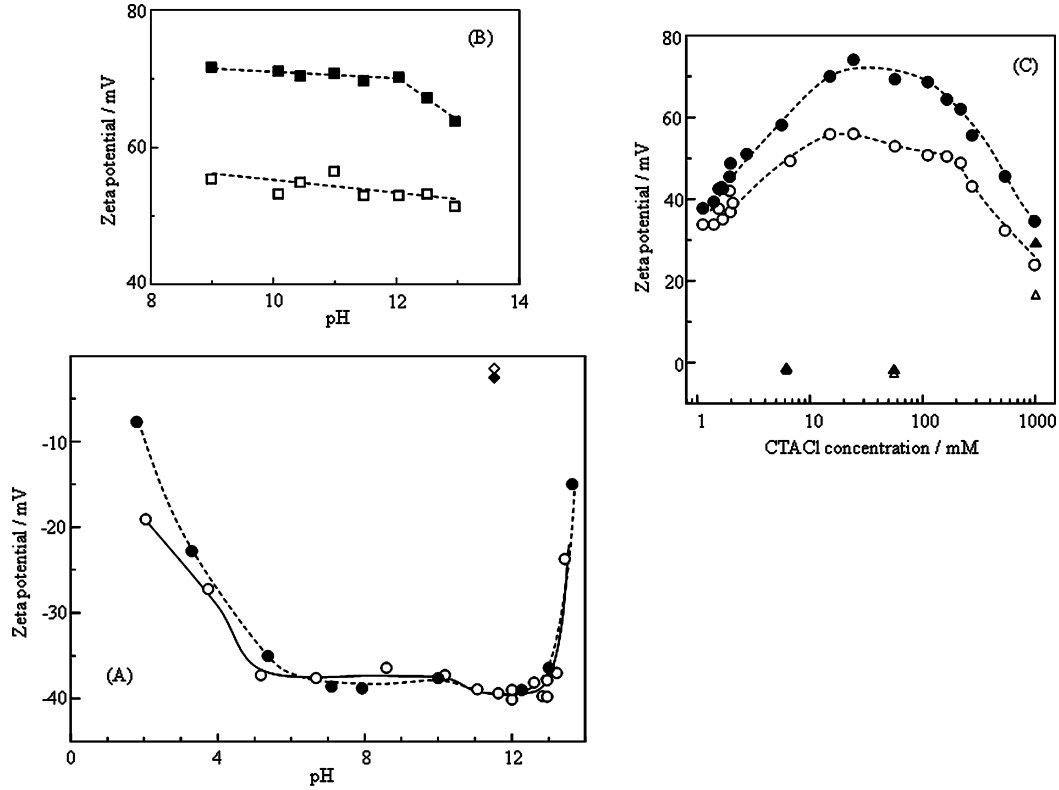

Figure 7. Zeta potential dependence of pH (A,B) and CTACl concentration (C). (A) ●, GO; ○, mGO; ◇, and 298 K; ◆, 348 K are for pure 57 mM CTACl solution; (B) □, 298 K; ■, 348 K for mGO + 57 mM CTACl; (C) ○, 298 K; ●, 348 K for mGO + CTACl while maintaining pH 11.7 for each solution; Δ, 298 K; ▲, 348 K are for pure CTACl solution with pH 11.7.

either the "salting-out" effect which destabilizes the colloidal solution or the increased opportunity of CTACl molecules to form cylinder micelles in the bulk solution.[51]

Functionality. Figure 8a shows the electrical conductivity of rGO−PMS(x) as a function of their carbon content. It is interesting that, in sharp contrast with the insulating property of the usual pure silica, these composites with PMS sandwiched rGO structure already showed a noticeable electrical conductivity at carbon content less than 5 wt %. The electrical conductivity increases from 0.04 to 4 $S \cdot m^{-1}$ when x increases from 0.027 to 4 mg/mL by which the carbon content goes up from 2.5 to 23 wt %. The values of 0.04−4 $S \cdot m^{-1}$ are much smaller than those of pure rGO materials (~2400 $S \cdot m^{-1}$)[18] but in the range typical of a semiconductor. This property is thus specific for the structure with the carbon component in the composites determining and improving the electrical conductivity. As discussed in the above sections, rGO layers are covered by the insulating PMS materials at both sides in rGO−PMS(0.27) synthesized at an optimum condition. It is likely that percolation occurs in the compacted pellet by connection of rGO layer edges of the closely contacted composite particles, which effects electron/hole transportation through the particles. The steep jump in electrical conductivity after $x = 2$ possibly reflects the stacking of more than one rGO layer in these composites containing greater carbon content (over 15 wt %) but poorer quality PMS structure (Figure S5c), which greatly increases the number of pathways for electrical conduction.

Figure 8b shows the adsorption isotherms of water and hexane at 303 K on rGO−PMS(0.27). Here the ordinate is expressed by the fractional ratio of pore filling which is defined as the hexane or water adsorption volume, V, divided by the pore volume, $V_0(N_2)$, from N_2 adsorption (Table 1). The $V/V_0(N_2)$ ratios are close to unity around $P/P_0 = 1$ for the two vapors, in agreement with the Gurvich rule,[43] indicating that the vapors are filled in mesopores by capillary condensation. The greater increase in pore filling of hexane as compared to water in the low P/P_0 range implies the hydrophobic property of the internal pore surface consisting of rGO layers and the surrounding cylindrical pores which contain a little carbon arising from the inert gas atmosphere used for template removal by sample pyrolysis. The greater low pressure hysteresis of water adsorption is indicative of formation of polar sites in the cylindrical pore walls which can induce dissociative adsorption of water. In parallel with the adsorption properties, the relative resistivity of rGO−PMS(0.27) dramatically decreases upon hexane adsorption and remains almost unchanged when hexane adsorption is saturated (Figure 8c). The smaller change of R/R_0 in the low P/P_0 range upon water adsorption is attributed to the small amount of water adsorption. In contrast, rGO−PMS(4) with a poor PMS structure and the pristine rGO films showed insig-

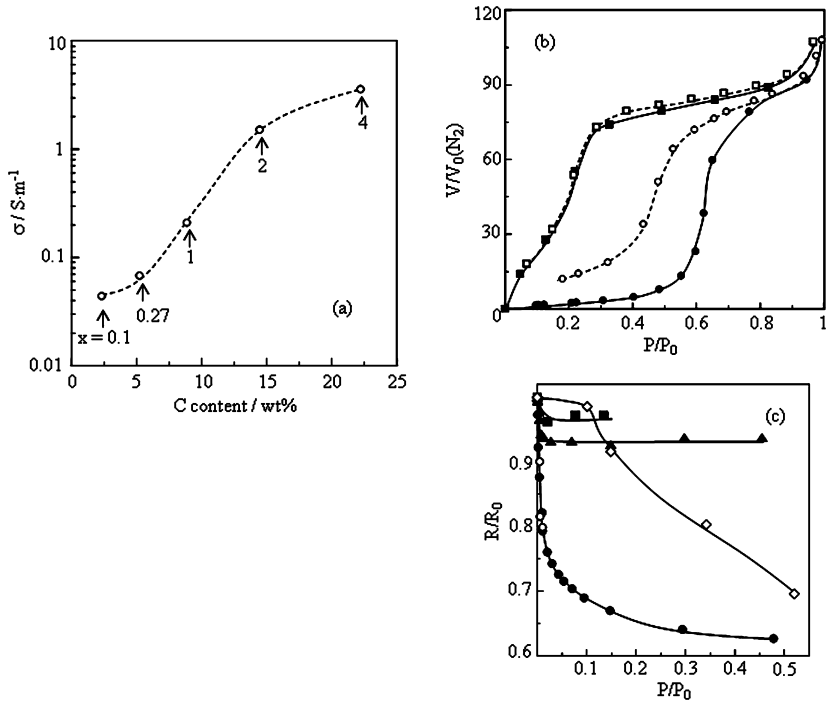

Figure 8. (a) Electrical conductivity of rGO−PMS(*x*) as a function of carbon content, (b) hexane (■, □) and H_2O (●, ○) adsorption isotherms on rGO−PMS(0.27) at 303 K where filled and unfilled marks are the adsorption and desorption branches, respectively, (c) change of relative resistance of rGO−PMS(0.27) (● with ○ representing the desorption process), rGO−PMS(4) (▲), and rGO film (■) exposed to hexane and that of rGO−PMS(0.27) exposed to H_2O (◇) at room temperature and different relative vapor pressure.

nificant change in R/R_0 upon vapor exposure despite a much better electrical conductivity (the measured sheet resistance for rGO film is ~1 kΩ per square). Therefore, the pronounced response of resistivity upon vapor exposure is considered to be a unique property of the rGO−PMS sandwich nanocomposite structure. The concentration of adsorbates in the vertically aligned mesopores and the direct contact of adsorbates with the semiconductive rGO bottom are the two most important factors responsible for the sensitive resistivity change observed. Since the changes in R/R_0 are reproducible, the observed behavior portends a promising opportunity for these rGO−PMS sandwich nanocomposites as effective sensors with molecule tunable selectivity with respect to both size and polarity.

Mode of Formation. It has been established that CTACl surfactants form hemispherical or spherical cylindrical micelles on atomically flat surfaces such as hydrophobic graphite or hydrophilic mica, respectively, under dilute CTACl concentration conditions.[52] These cylindrical micelles are found oriented parallel to the graphite and mica surfaces and moreover register with the underlying three-fold axes of the hexagonal symmetry lattices, termed meso-epitaxy. In earlier work, it proved possible to grow oriented hexagonal symmetry PMS film on graphite and mica, as well as free-standing PMS film at the water−air interface.[1,2,40] In the case of single-layer GO depending on the state of reduction, it is expected that surface charge, geometrical curvature, surface functional groups, surface polarity surface inhomogeneity, surface image charges in nanoscale aromatic domains, and double-sided surface cooperative effects may all influence the mode of formation of the graphene oxide−PMS sandwich structure, and the high stability of the mGO dispersion (Figure 7A) is a strong indicator that the surface chemistry of the mGO layer plays a major role in directing mGO/rGO−PMS structure formation.

Zeta potential results showed that single layers of mGO in solution are negatively charged under PMS synthesis conditions exposed to a highly basic environment. Thus, CTA^+ cations can be strongly adsorbed on mGO layers through an ion-exchange reaction, which then initialize the formation of micelle assemblies, namely, admicelles of the kind depicted in Figure 9a. These admicelles adhere to the mGO surface, thereby reversing the layer charge from negative to positive and stabilizing the mGO single layers in solution. The precise structure of the so-formed micelle aggregates on the surface of mGO is not clear; however, it is reasonable to expect the existence of spherical admicelles because the inhomogeneous distribution of surface groups and surface curvature of mGO resemble to some extent the rough and polar surface of amorphous silica on which spherical micelles have been reported.[52,53] The aforementioned surface complexity of mGO may not be conducive to the formation of well-ordered hexagonal arrays of cylindrical micelles oriented parallel to the surface of the kind observed on the perfectly flat surface of mica.[1] Figure 9a also illustrates the trimethyl-

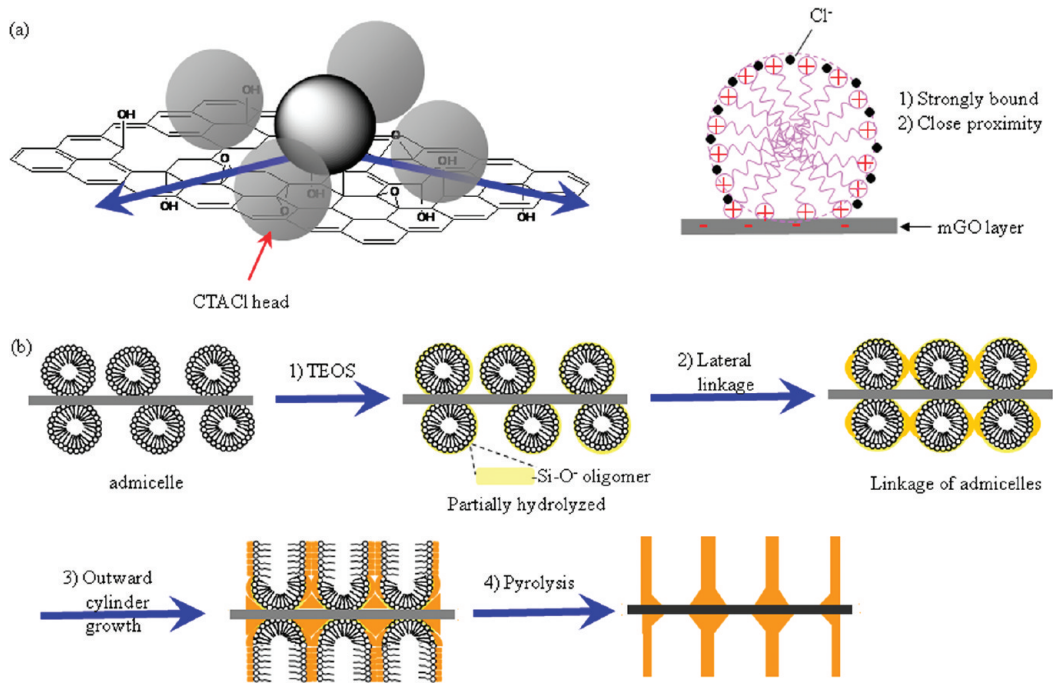

Figure 9. (a) Schematic representations of a CTACl headgroup (left) and an admicelle (right) on a mGO surface and (b) proposed mode of formation of rGO−PMS.

ammonium headgroup of the cationic CTA^+ surfactant relative to carbon rings on the surface of an mGO layer. Using a model of the hexagonal polyaromatic graphene lattice and assuming that mGO has a similar surface charge density to the parent GO (3−5 meq/g) as evidenced by zeta potential results, one reaches the conclusion that one CTA^+ headgroup (0.37−0.47 nm in size from a molecular model) covers ~3 carbon rings and 4−7 carbon rings (lateral size 1−1.7 nm) contain one surface charge on average.[54] This model pictures a very high surface charge density, which leads to the close proximity of admicelles and, possibly, the formation of quasi-hexagonally close-packed admicelles on the surface of mGO at the optimum pH, CTACl concentration, and temperature conditions (Figure 7).

When TEOS molecules are added into the CTA^+ preadsorbed mGO solution, they are rapidly hydrolyzed under the basic synthesis conditions to form monomeric, dimeric, and/or oligomerized negatively charged silicate species. These silicate species can (i) either be polymerized to large amorphous silica particles (species a) or (ii) bind to the positively charged CTA^+ headgroup in the bulk solution and form a PMS structure (species b) through the silicatropic co-assembly mechanism[50,55] or (iii) bind to the admicelles near the surface of mGO (species c). Although it has been reported that pH 11−12 is appropriate to form hexagonal symmetry PMS,[50] the control synthesis results showed that the lower silica to surfactant ratio used in this study did not support sufficient polymerization of silicate species and the growth of PMS in solution. The formation of species a is also disfavored at a smaller silica to surfactant ratio. Since the CTA^+ admicelles are highly charged, species c can be formed preferentially compared to species a and b, and as a result, silicate species quickly gather around admicelles in close proximity to mGO layers, (1) in Figure 9b. As the admicelles are close to one another, further polymerization of silicate leads to linkage of neighboring admicelles on the mGO surface. Considering the surface inhomogeneity of mGO, this process possibly involves surface diffusion and silicate polymerization among admicelles, (2) of Figure 9b. The act of co-assembling CTA^+ with the silicate species and their subsequent polymerization may induce a structural transformation of spherical admicelles to cylindrical ones growing normal to the surface of mGO,[56] (3) of Figure 9b. In other words, growth of the vertically aligned channels of the PMS film on the surface of mGO could be triggered by the formation of close-packed admicelles or silicatropic admicelles. The formation of a well-polymerized and rigid PMS structure on both surfaces of mGO platelets before removal of CTACl can account for the negligible contraction in d_{100} spacing after thermal post-treatment, (4) of Figure 9b. This model for the mode of formation predicts that PMS with channels oriented vertically with respect to an mGO thin film can be synthesized under similar conditions. Our results of preliminary experiments on the growth of PMS on mGO thin films confirmed this prediction. Further experiments of this genre are ongoing in our laboratory.

CONCLUSIONS

Mild reduction of single-layer GO in basic solution maintains a stable colloidal dispersion in which the oxygen-containing groups and the structure of carbon

were modified. This modification process involves loss of carbon and consumption of hydroxide in solution for the reaction. The modified GO serves as a novel template for the self-assembly and growth of PMS films on both sides of the GO, forming the first example of a sandwich reduced graphene oxide−periodic mesoporous silica nanocomposite in which the channels are oriented perpendicularly to the surface of rGO platelets. The unexpected vertical mesopore alignment of the PMS film on the GO/rGO was established by a combination of PXRD, SEM/TEM, and N_2 adsorption techniques. The formation of the nanocomposite is very sensitive to pH and influenced by the CTACl/mGO concentrations, the amount of TEOS, and synthesis temperature. The results of zeta potential measurements reveal the charge inversion of zeta potential when CTACl is added in mGO solution, indicating the preadsorption of CTACl and admicelle assembly on the surface of mGO. A tentative admicelle-initiated growth model is proposed to rationalize the experimental observations. It is considered essential that CTACl admicelles are strongly attached to the surface of GO and are in close proximity in order to direct the assembly of a PMS coating with a vertically aligned channel structure with respect to the GO surface. The nanocomposites showed semiconductive behavior with electrical conductivity sensitively responding to analyte vapor pressure. The new nanocomposites unraveled in this study bode well for many different kinds of basic and applied research opportunities that take advantage of the synergistic integration of GO and PMS into reduced graphene oxide−PMS sandwich structures, such as sensing with molecule tunable selectivity, patterning through self-assembly, electrically stimulated drug delivery, mesochannel membrane for electrochemical growth of short metal nanorods and barcode metal nanorods.

EXPERIMENTAL METHODS

GO and Modification. GO was prepared from natural graphite by the Hummer−Offeman's method.[57] The chemical composition was found to be $C_8O_{4.3}H_{0.7}$ as determined by elemental analysis (obtained by subtracting the H_2O content determined by thermal gravimetric analysis, TGA). Acid−base titration using diluted alkaline solutions of GO (containing sodium chloride as charge balancing electrolyte) usually gave a very high cation exchange capacity, in the range of 3−5 meq/g for GO, depending on preparation methods and batches.[58−62]

For the synthesis of modified GO dubbed mGO, powders of GO were first immersed in a diluted NaOH solution (0.014−0.05 M) in a polypropylene (PP) bottle to form a mixture (GO content: 0.27−2.0 mg/mL, pH 11.8−12.8). After sonication for 1 h, the mixture became a stable colloidal dispersion with the expected brown color and was then heated in an oil bath at 353 K for 12 h. The PP bottle was tightly sealed during the sonication and thermal treatment so that the solvent did not evaporate and the total volume of the dispersion remained the same. After the thermal treatment, the dispersion became dark gray with a mild brownish tinge and remained a colloidally stable dispersion for months.

To determine the content of mGO in solution, several droplets of HCl (1/10) solution were added to a fixed quantity of the dispersion to precipitate mGO. The mGO aggregates were collected by filtration, thoroughly washed with distilled water to pH 6−7, and dried in vacuum at 333 K before weighing. The dry mGO powders were kept under nitrogen for elemental analysis.

Nanocomposite Synthesis. Cetyltrimethylammonium chloride (CTACl, 25 wt % aqueous solution) and tetraethoxysilane (TEOS, reagent grade 98%) were purchased from Aldrich. Sodium hydroxide (Pellets Pastilles) was purchased from ACP Chemicals Inc. A typical synthesis of GO−PMS nanocomposite was carried out as follows. CTACl (0.102 mol) was first added into an mGO dispersion (100 mol H_2O, initial GO content: 0.027−4 mg/mL). The mGO dispersion can be prepared directly or by diluting a concentrated mGO dispersion with distilled water. The pH of the dispersion was adjusted by adding several droplets of NaOH solution (1 M) or HCl solution (1/10), and the mixture was magnetically stirred in room temperature (RT) and further at 353 K for 80 min. After the dispersion was cooled to RT, TEOS (0.128 mol) was dropwise delivered into the solution. The resulting mixture was heated at 353 K for 24 h, and the precipitate was collected by centrifugation and aged at RT overnight and at 353 K for 24 h. Throughout the experiment, the PP container bottle was tightly sealed except when reagents were added. The as-synthesized dry powders (denoted by mGO−PMS(x) where x is for the initial GO content) were thermally treated under N_2 atmosphere at 773 K for 3 h (ramp rate 1 K/min) to give the nanocomposite containing further reduced graphene oxide (rGO) layers. This nanocomposite (denoted by rGO−PMS(x)) has a dark color, reflective of the carbonization of mGO layers during the thermal pyrolysis. The pH after CTACl addition, the CTACl concentration, the amount of TEOS, the mGO concentration, and the reaction temperature were varied. Other conditions were not changed when varying one of these conditions except when otherwise mentioned.

Characterization. Powder X-ray diffraction (PXRD) patterns were collected on an automated Bruker/Siemens AXS D5000 diffractomter with a $\theta/2\theta$ Bragg−Brentano reflection geometry with fixed slits. The system is equipped with a high power line focus Cu Kα source operating at 50 kV and 35 mA. A solid-state Si/Li Kevex detector was used for removal of unwanted Kβ lines. A step scan mode was used for data acquisition, and the scanning range was set up within the interval of $2\theta = 0.8-5.0°$ with step size of 0.02° and counting time of 3.0 s per step. Slits were set up appropriately according to the scanned range in order to ensure maximum peak-to-noise ratio.

Scanning and transmission electron microscopy (SEM and TEM) was carried out on both a Hitachi S-5200 SEM equipped with a TE detector, operating at 30 kV and a Hitachi HD-2000 dedicated STEM equipped with a SE detector operating at 200 kV. Samples embedded in Epon epoxy resin were microtomed to thin sections of about 20−100 nm.

UV−vis spectra were collected on a Varian CARY 100 BIO UV−vis spectrophotometer. GO dispersion in NaOH (0.05M) and mGO dispersion thereafter prepared were diluted with distilled water to an appropriate absorbance range, and their normalized spectra were compared.

FT-IR spectra were measured on a Perkin-Elmer spectrometer. Solvent dispersions or water slurries of samples were drop-casted onto nondoped Si wafers, and the measurements were carried out in the 400−4000 cm^{-1} range with a resolution of 4 cm^{-1}. A nondoped Si wafer was used as the background.

Raman spectra were recorded on a Horiba Jobin Yvon LabRam Raman microscope with a 532 nm excitation source and a 100× (0.8 NA) microscope objective at resolution of 2 cm^{-1}. Drop-casted sample films on nondoped Si wafers were used for the measurement.

N_2 adsorption was carried out at 77 K by a Quantachrome Autosorp-1 volumetric apparatus. Hexane and water adsorption were carried out at 303 K using a Japan Bell Co. volumetric appa-

ratus. Samples were pre-evacuated sufficiently at RT and further at 393 K for 3 h before adsorption.

Zeta potentials were measured on a Malvern Zetasizer 3000 HAS instrument at both 298 and 348 K. Dispersions of GO (1 mg/mL) and mGO (from 1 mg/mL GO solution) were diluted by 40-fold into the appropriate concentration range for the measurement by using aqueous NaOH solution or pure distilled water. The pH of the diluted solution was further adjusted by droplets of NaOH solution (0.05 M) or HCl solution (1/20). No difference in zeta potential was observed for mGO dispersions from different original concentration but at the same dilution level (1/40). For the mGO and CTACl mixture solution, the solution was prepared in such a way that either the concentrations of mGO (1/40 dilution) and CTACl (57 mM (1.76 wt %)) were maintained while only pH was changed from 9 to 13 or the pH value and mGO concentration were maintained while the CTACl concentration was changed from 1.12 mM (0.036 wt %) to 992 mM (24 wt %). The difference in concentration upon pH adjustment was negligible except for the pH 13 one in which the CTACl concentration was reduced to 52 mM.

Thermal gravimetric analysis (TGA) was measured on a TA Instruments SDT Q600 under N_2 atmosphere (200−250 mL/min) at a ramp rate of 1 K/min. An α-Al_2O_3 pan was used as the reference.

Elemental analysis was carried out by a PerkinElmer 2400 Series II CHNS analyzer. The electrical conductivity of the composites was measured by the four-probe method after pressing the sample powders to a rectanglar pellet with a density of 1.2−1.5 g mL^{-1}. The sensing properties of the composites were examined at room temperature (295−298 K) with a homemade setup which allows introduction and evacuation of analyte vapor and real-time analyzing of vapor pressure and electrical conductivity.

Acknowledgment. G.A.O. is Government of Canada Research Chair in Materials Chemistry and Nanochemistry. He is deeply indebted to the Natural Sciences and Engineering Council of Canada for strong and sustained support of his research. Z.M.W. thanks the bilateral researcher exchange program of the Japan Society for the Promotion of Science (JSPS) for financial support. We are indebted to Dr. T. Seki for technical assistance with the preparation of GO. Dr. S. Petrov is acknowledged for collecting PXRD data. Dr. J. Vickery and Dr. K. Liu are acknowledged for technical support and valuable discussions on zeta potential measurements. We thank Ms. S. Mamiche for laboratory technical support.

Supporting Information Available: FT-IR and additional Raman spectra, TGA curves, STEM cross-sectional elemental mapping analysis, additional TEM image, and PXRD patterns at different synthesis conditions included. This material is available free of charge *via* the Internet at http://pubs.acs.org.

REFERENCES AND NOTES

1. Yang, H.; Kuperman, A.; Coombs, N.; Mamiche-Afara, S.; Ozin, G. A. Synthesis of Oriented Mesoporous Silica Films on Mica. *Nature* **1996**, *379*, 703–705.
2. Yang, H.; Coombs, N.; Sokolov, I.; Ozin, G. A. Registered Growth of Mesoporous Silica Films on Graphite. *J. Mater. Chem.* **1997**, *7*, 1285–1290.
3. Aksay, I. A.; Trau, M.; Manne, S.; Honma, I.; Yao, N.; Zhou, L.; Fenter, P.; Eisenberger, P. M.; Gruner, S. M. Biomimetic Pathways for Assembling Inorganic Thin Films. *Science* **1996**, *273*, 892–898.
4. Zhao, D.; Yang, P.; Melosh, N.; Feng, J.; Chmelka, B. F.; Stucky, G. D. Continuous Mesoporous Silica Films with Highly Ordered Large Pore Structures. *Adv. Mater.* **1998**, *10*, 1380–1385.
5. Sokolov, I.; Yang, H.; Ozin, G. A.; Henderson, G. S. Beyond the Hemimicellar Cylindrical Monolayer on Graphite: AFM Evidence for Lyotropic Liquid Crystal Film. *Adv. Mater.* **1997**, *9*, 917–921.
6. Walcarius, A.; Sibottier, E.; Etienne, M.; Ghanbaja, J. Electrochemically Assisted Self-Assembly of Mesoporous Silica Thin Films. *Nat. Mater.* **2007**, *6*, 602–608.
7. Yamaguchi, A.; Uejo, F.; Yoda, T.; Uchida, T.; Tanamura, Y.; Yamashita, T.; Teramae, N. Self Assembly of Silica−Surfactant Nanocomposite in Porous Alumina. Membrane. *Nat. Mater.* **2004**, *3*, 337–341.
8. Koganti, V. R.; Dunphy, D.; Gowrishankar, V.; McGehee, M. D.; Li, X.; Wang, J.; Rankin, S. E. Generalized Coating Route to Silica and Titania Films with Orthogonally Titled Cylindrical Nanopore Arrays. *Nano Lett.* **2006**, *6*, 2567–2570.
9. Richman, E. K.; Brezesinski, T.; Tolbert, S. H. Vertically Oriented Hexagonal Mesoporous Films Formed through Nanometer Scale Epitaxy. *Nat. Mater.* **2008**, *7*, 712–717.
10. Yang, H.; Ozin, G. A.; Kresge, C. T. The Role of Defects in the Formation of Mesoporous Silica Fibers, Films, and Curved Shapes. *Adv. Mater.* **1998**, *10*, 883–887.
11. Yang, P.; Wirnsberger, G.; Huang, H. C.; Cordero, S. R.; McGehee, M. D.; Scott, B.; Deng, T.; Whitesides, G. M.; Chmelka, B. F.; Buratto, S. K.; *et al.* Mirrorless Lasing from Mesostructured Waveguides Patterned by Soft Lithography. *Science* **2000**, *287*, 465–467.
12. Prado, R.; Beobide, G.; Marcaide, A.; Goikoetxea, J.; Aranzabe, A. Development of Multifunctional Sol−Gel Coatings: Anti-reflection Coatings with Enhanced Self-Cleaning Capacity. *Sol. Energy Mater. Sol. Cells* **2010**, *94*, 1081–1088.
13. Landskron, K.; Hatton, B. D.; Perovic, D. D.; Ozin, G. A. 3-Rings of SiO_2C_2 Tetrahedra as Building Units of Periodic Mesoporous Organosilicas. *Science* **2003**, *302*, 266–269.
14. Hatton, B. D.; Landskron, K.; Whitnall, W.; Perovic, D. D.; Ozin, G. A. Spin-Coated Periodic Mesoporous Organosilica Thin-Films—Towards a New Generation of Low-Dielectric-Constant Materials. *Adv. Funct. Mater.* **2005**, *15*, 823–829.
15. Wang, W. D.; Grozea, D.; Kim, A.; Perovic, D. D.; Ozin, G. A. Vacuum-Assisted Aerosol Deposition of a Low-Dielectric-Constant Periodic Mesoporous Organosilica Film. *Adv. Mater.* **2010**, *22*, 99–102.
16. Choi, S. Y.; Mamak, M.; Von Freymann, G.; Chopra, N.; Ozin, G. A. Mesoporous Bragg Stack Color Tunable Sensors. *Nano Lett.* **2006**, *6*, 2456–2461.
17. Chen, H. T.; Crosby, T. A.; Park, M. H.; Nagarajan, S.; Rotello, V. M.; Watkins, J. J. Accessibility of Cylindrical Channels within Patterned Mesoporous Silica Films Using Nanoparticle Diffusion. *J. Mater. Chem.* **2009**, *19*, 70–74.
18. Dreyer, D. R.; Park, S.; Bielawski, C. W.; Ruoff, R. S. The Chemistry of Graphene Oxide. *Chem. Soc. Rev.* **2010**, *39*, 228–240.
19. Compton, O. C.; Nguyen, S. T. Graphene Oxide, Highly Reduced Graphene Oxide, and Graphene: Versatile Building Blocks for Carbon-Based Materials. *Small* **2010**, *6*, 711–723.
20. Eda, G.; Chhowalla, M. Chemically Derived Graphene Oxide: Towards Large-Area Thin-Film Electronics and Optoelectronics. *Adv. Mater.* **2010**, *22*, 2392–2415.
21. Allen, M. J.; Tung, V. C.; Kaner, R. B. Honeycomb Carbon: A Review of Graphene. *Chem. Rev.* **2010**, *110*, 132–145.
22. Chiang, H. L.; Huang, C. P.; Chiang, P. C. The Surface Characteristics of Activated Carbon as Affected by Ozone and Alkaline Treatment. *Chemosphere* **2002**, *47*, 257–265.
23. Fan, X.; Peng, W.; Li, Y.; Li, X.; Wang, S.; Zhang, G.; Zhang, F. Deoxygenation of Exfoliated Graphite Oxide under Alkaline Conditions: A Green Route to Graphene Preparation. *Adv. Mater.* **2008**, *20*, 4490–4493.
24. Ang, P. K.; Wang, S.; Bao, Q; Thong, J. T. L.; Loh, K. P. High-Throughput Synthesis of Graphene by Intercalation−Exfoliation of Graphite Oxide and Study of Ionic Screening in Graphene Transistor. *ACS Nano* **2009**, *3*, 3587–3594.
25. Li, D.; Müller, M. B.; Gilje, S.; Kaner, R. B.; Wallace, G. G. Processable Aqueous Dispersions of Graphene Nanosheets. *Nat. Nanotechnol.* **2008**, *3*, 101–105.
26. Stankovich, S.; Piner, R. D.; Chen, X.; Wu, N.; Nguyen, S. T.; Ruoff, R. S. Stable Aqueous Dispersions of Graphitic Nanoplatelets *via* the Reduction of Exfoliated Graphite Oxide in the Presence of Poly(sodium 4-styrenesulfonate). *J. Mater. Chem.* **2006**, *16*, 155–158.

27. Dresselhaus, M. S.; Hofmann, A. J., M.; Dresselhaus, G.; Saito, R. Perspectives on Carbon Nanotubes and Graphene Raman Spectroscopy. *Nano Lett.* **2010**, *10*, 751–758.
28. Kudin, K. N.; Ozbas, B.; Schniepp, H. C.; Prud'homme, R. K.; Aksay, I. A.; Car, R. Raman Spectra of Graphite Oxide and Functionalized Graphene Sheets. *Nano Lett.* **2008**, *8*, 36–41.
29. Jung, I.; Dikin, D. A.; Piner, R. D.; Ruoff, R. S. Tunable Electrical Conductivity of Individual Graphene Oxide Sheets Reduced at "Low" Temperatures. *Nano Lett.* **2008**, *8*, 4283–4287.
30. Wei, Z.; Barlow, D. E.; Sheehan, P. E. The Assembly of Single-Layer Graphene Oxide and Graphene Using Molecular Templates. *Nano Lett.* **2008**, *8*, 3141–3145.
31. Tuinstra, F.; Koenig, J. L. Raman Spectrum of Graphite. *J. Chem. Phys.* **1970**, *53*, 1162–1130.
32. Lerf, A.; He, H.; Forster, M.; Klinowski, J. Structure of Graphite Oxide Revisited. *J. Phys. Chem. B* **1998**, *102*, 4477–4482.
33. Scholz, W.; Boehm, H. P. Untersuchungen am Graphitoid. VI Betrachtungen zur Struktur des Graphitoxids. *Z. Anorg. Allg. Chem.* **1969**, *369*, 327–340.
34. Szabó, T.; Berkesi, O.; Forgo, P.; Josepovits, K.; Sanakis, Y.; Petridis, D.; Dékány, I. Evolution of Surface Functional Groups in a Series of Progressively Oxidized Graphite Oxides. *Chem. Mater.* **2006**, *18*, 2740–2749.
35. Wang, Z.-M.; Hoshinoo, K.; Shishibori, K.; Kanoh, H.; Ooi, K. Surfactant-Mediated Synthesis of a Novel Nanoporous Carbon−Silica Composites. *Chem. Mater.* **2003**, *15*, 2926–2935.
36. The powder samples collected from mGO dispersion cannot be easily redispersed even in basic solution, possibly indicating that the surface groups of mGO are somehow temporarily stabilized in basic solution.
37. Yang, H.; Vovk, G.; Coombs, N.; Sokolov, I.; Ozin, G. A. Synthesis of Mesoporous Silica Spheres under Quiescent Aqueous Acidic Conditions. *J. Mater. Chem.* **1998**, *8*, 743–750.
38. Kresge, C. T.; Leonowicz, M. E.; Roth, W. J.; Vartuli, J. C.; Beck, J. S. Ordered Mesoporous Molecular Sieves Synthesized by a Liquid-Crystal Template Mechanism. *Nature* **1992**, *359*, 710–712.
39. Beck, J. S.; Vartuli, J. C.; Roth, W. J.; Leonowicz, M. E.; Kresge, C. T.; Schmitt, K. D.; Chu, C. T -W.; Olson, D. H.; Sheppard, E. W.; McCullen, S. B.; *et al.* A New Family of Mesoporous Molecular Sieves Prepared with Liquid Crystal Templates. *J. Am. Chem. Soc.* **1992**, *114*, 10834–10843.
40. Yang, H.; Coombs, N.; Sokolov, I.; Ozin, G. A. Free-Standing and Oriented Mesoporous Silica Films Grown at the Air−Water Interface. *Nature* **1996**, *381*, 589–592.
41. Firouzi, A.; Atef, F.; Oertli, A. G.; Stucky, G. D.; Chmelka, B. F. Alkaline Lyotropic Silicate−Surfactant Liquid Crystals. *J. Am. Chem. Soc.* **1997**, *119*, 3596–3610.
42. The π-conjugated carbon structure in rGO−PMS(0.27) (pH 11.7) was further restored as evidenced by Raman spectra (Figure S1B), which showed a reduced I_D/I_G ratio, and FT-IR spectrum (Figure S1A), which showed a−C═C−absorption at a similar position to that of pyrolysed mGO (~1571 cm^{-1}). An ambiguous 2D (G′) band in its Raman spectrum is centered at a position close to that of graphene.[27] The terminal Si−OH groups observed in its FT-IR spectrum indicate formation of highly developed silica structure.
43. Gregg, S. J.; Sing, K. S. W. *Adsorption, Surface Area, and Porosity*; Academic: New York, 1982.
44. Rouquerol, F.; Rouquerol, J.: Sing, K. S. W. *Adsorption by Powders & Porous Solids*; Academic: San Diego, CA, 1999.
45. Thommes, M.; Köhn, R.; Fröba, M. Sorption and Pore Condensation Behavior of Pure Fluids in Mesoporous MCM-48 Silica, MCM-41 Silica, SBA-15 Silica and Controlled-Pore Glass at Temperatures above and below the Bulk Triple Point. *Appl. Surf. Sci.* **2002**, *96*, 239–249.
46. Sing, K. S. W.; Everett, D. H.; Haul, R. A. W.; Moscou, L.; Pierotti, R. A.; Rouquerol, J.; Siemieniewska, T. Reporting Physisorption Data for Gas/Solid Systems with Special Reference to the Determinations of Surface Area and Porosity. *Pure Appl. Chem.* **1985**, *57*, 603–619.
47. Seaton, N. A.; Walton, J. R. B.; Quirke, N. A New Analysis Method for the Determination of the Pore Size Distribution of Porous Carbons from Nitrogen Adsorption Measurements. *Carbon* **1989**, *27*, 853–861.
48. Thommes, M. In *Nanoporous Materials, Science & Engineering*; Lu, G. Q., Zhao, X. S., Eds.; Imperial College Press: London, 2004; Chapter 11, pp 318−364.
49. A more appropriate value is 0.135 nm^2 for the cross-sectional area (σ_{N2}) of the N_2 molecule than the usual 0.162 nm^2 when the BET method is applied to solids with a polar surface such as zeolite. S_{BET}* from $\sigma_{N2} = 0.135$ nm^2 better matches S_{DFT}. The larger $V_{0,DFT}$ value of G-PMS (pH 11.7) is related to its greater mesopore size.
50. Monnier, A.; Schuth, F.; Huo, Q.; Kumar, D.; Margolese, D.; Maxwell, R. S.; Stucky, G. D.; Krishnamurty, M; Petroff, P.; Firouzi, A.; *et al.* Cooperative Formation of Inorganic−Organic Interfaces in the Synthesis of Silicate Mesostructures. *Science* **1993**, *261*, 1299–1303.
51. According to Israelachvili *et al.*, micelle structure in bulk solution can be considered from the point of view of geometric constraints and a dimensionless parameter g for determining the preferred surfactant aggregate configuration, described as V/A_0l_c, where V is the volume occupied by hydrophobic group in a micelle core, A_0 is the mean cross-sectional area per hydrophilic headgroup at the micelle surface, and l_c is the characteristic length of hydrophobic chain. Spherical micelles form when $g < 1/3$, cylinder micelles when $1/3 < g < 1/2$, bilayers or vesicles when $1/2 < g < 1$, and inverted micelles when $g > 1$. In other words, an increased g value implies that the surfactant tends to adopt a higher order aggregate configuration. Since excess OH^- at high pH reduces the electrostatic repulsion between hydrophilic headgroups, thus increasing the g value by decreasing A_0, the significant increase in zeta potential of the basic CTACl bulk solution (~1000 mM) in Figure 7C can be attributed to the formation of cylindrical micelle aggregates whose sizes are large enough to be detected by the zeta potential equipment (20−900 nm). Here higher temperature contributes more to the tendency toward micelle formation due to dehydration of CTA^+ hydrophilic head (Myers, D. *Surfactant Science and Technology*; Wiley-Interscience: New York, 1996). Israelachvili, J. N.; Mitchell, D. J.; Ninham, B. W. *J. Chem. Soc., Faraday Trans. 2* **1976**, *72*, 1525–1568.
52. Manne, S.; Gaub, H. E. Molecular Organization of Surfactants at Solid−Liquid Interfaces. *Science* **1993**, *270*, 1480–1482.
53. Schulz, J. C.; Warr, G. G. Adsorbed Layer Structure of Cationic Surfactants on Quartz. *Phys. Rev. E* **2001**, *63*, 0416041-5.
54. Irrespective of the still undetermined structure of GO and different levels of reduced GO, all of the GO structural models up to now consider cyclohexane/cyclohexene rings or the remains of aromatic rings, allowing a rough approximation of the surface using the graphene geometry for GO/mGO layer dimensions. A more realistic approximation may be obtained from the reported surface charge density values in the range 0.7−2 charges/nm^2 (refs 58 and 62, where GO was prepared by Brodie's method). Considering a CTACl micelle diameter of about 5−6 nm, this indicates that one micelle covers 10−57 charges, which still shows a very strong interaction between admicelles and the GO/mGO surface.
55. Firouzi, A.; Kumar, D.; Bull, L. M.; Besier, T.; Sieger, P.; Huo, Q.; Walker, S. A.; Zasadzinski, J. A.; Glinka, C.; Nicol, J.; *et al.* Cooperative Organization of Inorganic-Surfactant and Biomimetic Assemblies. *Science* **1995**, *267*, 1138–1143.
56. One optional explanation for transformation of spherical micelles to cylinder aggregates can be made *via* the silicatropic mechanism which was adopted by Monnier *et al.*[50] to explain the formation mechanism of a bulk PMS structure under alkaline conditions. According to this

consideration, binding of CTA^+ with silicate oligomers with appropriate surface charges and geometrical sizes will trigger cylindrical self-assembling determined by the *g* value.[51] Binding of admicelles with silicate oligomers (formation of species c) and their subsequent polymerization may create a chemical environment similar to bulk phase cylindrical self-assembling, although the admicelles take spherical ordering at the initial stage. As the bottom half of the admicelles is fixed by strong interaction with the mGO surface and by lateral cross-linkage with the neighboring admicelles, the self-assembled cylinders can grow only off the upper part of admicelles but on the basis of lower part of the admicelles. This tendency is enhanced when admicelles tend to accommodate more CTA^+-binding silicate oligomers formed in bulk solution. However, future work is needed to figure out the detailed admicelles structure and the formation mechanism.

57. Hummers, W. S.; Offeman, R. E. Preparation of Graphite Oxides. *J. Am. Chem. Soc.* **1958**, *80*, 1339.
58. Dékány, I.; Krüger-Grasser, R.; Weiss, A. Selective Liquid Sorption Properties of Hydrophobized Graphite Oxide Nanostructures. *Colloid Polym. Sci.* **1998**, *276*, 570–576.
59. Cassagneau, T.; Guérin, F.; Fendler, J. H. Preparation and Characterization of Ultrathin Films Layer-by-Layer Self-Assembled from Graphite Oxide Nanoplatelets and Polymers. *Langmuir* **2000**, *16*, 7318–7324.
60. Chu, Y.-H; Wang, Z.-M; Yamagishi, M.; Kanoh, H.; Hirotsu, T.; Zhang, Y.-X. Synthesis of Nanoporous Graphite-Derived Carbon−Silica Composites by a Mechanochemical Intercalation Approach. *Langmuir* **2005**, *21*, 2545–2551.
61. Liu, Y.-J.; Wang, Z.-M.; Aizawa, M.; Peng, W.-Q.; Hirotsu, H. Nanoporous Composite of Carbon Nanosheets and Functional Titania Nanoparticles Formed by Reassembling of Exfoliated Graphite Oxides with Colloidal Titania. *Mater. Lett.* **2009**, *63*, 260–262.
62. Szabó, T.; Tombácz, E.; Illés, E.; Dékány, I. Enhanced Acidity and pH-Dependent Surface Charge Characterization of Successively Oxidized Graphite Oxides. *Carbon* **2006**, *44*, 537–545.